Multi-component (Ag-Au-Cu-Pd-Pt) Alloy Nanoparticles Decorated p-type 2D-Molybdenum Disulphide (MoS_2) for Enhanced Hydrogen Sensing

Kusuma Urs MB[1#], Nirmal Kumar Katiyar[2#], Ritesh Kumar[3], Krishanu Biswas[2*], Abhishek K. Singh[3*], C S Tiwary[4*] and Vinayak Kamble[1*]

[1] *School of Physics, Indian Institute of Science Education and Research, Thiruvananthapuram, Kerala -695551 INDIA*

[2]*Department of Materials Science and Engineering, Indian Institute of Technology Kanpur, Kanpur-208016 INDIA*

[3]*Materials Research Centre, Indian Institute of Science, Bangalore, Karnataka-560012, INDIA*

[4]*Metallurgical and Materials Engineering, Indian Institute of Technology Kharagpur, Kharagpur-382355, INDIA*

Abstract

Molybdenum Disulphide (MoS_2) has emerged as a promising material for the development of efficient sensors. Here, we have exfoliated and decorated MoS_2 flakes with the novel, single-phase multi-component (Silver-Gold-Cupper-Palladium-Platinum (Ag-Au-Cu-Pd-Pt)) popularly named as high Entropy Alloy (HEA) nanoparticles using facile and scalable low-temperature grinding, followed by sonochemical method. It is found that the decoration of HEA nanoparticles imparts surface-enhanced Raman scattering effect and reduction in the work function of the material from 4.9 to 4.75 eV as measured by UV photoelectron spectroscopy. This change in the work function results in a schottky barrier between the gold contact and HEA decorated MoS_2 flakes as a result of drastic changes in the surface chemical non-stoichiometry. The response to hydrogen gas is studied at temperatures 30 to 100 ^oC, and it shows unusual *p*-type nature due to surface adsorbed oxygen species. The nanoscale junction formed between HEA and MoS_2 shows a 10 times increase in the response towards hydrogen gas at 80 ^oC. The experimental observations have been explained with DFT simulation showing more favourable hydrogen adsorption on HEA decorated MoS_2 resulting in an enhanced response.

Keywords: *MoS_2 nanosheets, high entropy alloys (Ag-Au-Cu-Pd-Pt), Schottky Junction, hydrogen sensing, Microscopy.*

#equal contribution
Email: kbvinayak@iisertvm.ac.in, chandra.tiwary@metal.iitkgp.ac.in, kbiswas@iitk.ac.in, abhishek@iisc.ac.in

Introduction

The high surface area of the atomically thin materials (2D materials) utilized for different kinds of applications starting from electronics, energy generation, biomedical, and sensors[1-5]. Further, the varied and tunable electronic properties of these materials make them a hot cake for various optoelectronic applications. The Transition Metal Dichalcogenides (TMDs) are one of the exciting family of 2D materials, which are reported to be interesting for their varied physical and chemical properties[6]. Particularly in the area of chemical sensors, with the discovery of graphene and TMDs, the onus has been shifted from metal oxide materials to them due to their excellent sensing properties such as sensitivity at relatively low operating temperatures[7]. Hydrogen (H_2) is a low density, colourless, odourless gas. It has an extensive flammability range (4-75%) by volume in air, and it has a vast utility as a fuel space as well as territorial applications[8]. Hence, it is essential to monitor the possible leakage at low temperatures as well as lower concentrations with high sensitivity. Most of the metal oxide semiconductor-based H_2 sensors operated at much higher temperatures ($> 200\ ^oC$)[9]. Therefore, a suitable low operating temperature sensor device is required, which can be energy efficient and used without a power-hungry heater assembly. The high chemical sensitivity of the molybdenum disulfides is utilized for the development of a different class of gas sensors[7, 10,11]. In contrast to the bulk TMDs, the fact they can be exfoliated into individual layers of a single atom thick sheets makes them far more responsive than that of the bulk counterpart. These individual layers of MoS_2 (or any TMDs) are stacked in bulk employing weak Van der Waals forces and hence can be easily exfoliated. These single sheets have a much higher surface area as well as active sites like edges, vacancies, dangling bonds, etc; hence have a much larger change in the conductivity as a result of surface adsorption of gases[6]. However, the major issue of the MoS_2 based sensors is their lower sensitivities and large response time, i.e., time taken by sensor to reach 90% of the saturation for a given concentration of gas as well as recovery

time, i.e., time taken to come back to 90% of the saturation value upon withdrawing the test gas. This large recovery times arise due to high binding energies of the gas molecules on to the highly reactive MoS_2 surface[7, 12]. This could be addressed by making heterostructures of MoS_2 with different materials having better electronic properties such as- nanoparticles of metals, alloys, oxides, other chalcogenides, etc[5]. However, the methods of synthesis of such heterostructures are quite complicated and involve multistep. Thus, a simple, facile, and scalable method is always desirable.

Recently developed, multicomponent High Entropy Alloys (HEA) have attracted a lot of attention due to its unique properties, which are distinctly different than that of its individual components[13, 14]. The structural stability and high chemical activity of these HEA have been utilized in structural and energy generation applications. Recent literature reported the combination of strong (Pd, Pt) and weak (Ag, Au) absorption strengths of hydrogen, AgAuCuPdPt alloy has excellent catalytic activity in electro-reduction of formic acid, towards the production of CO_2 and H_2 even at zero bias[15, 16]. Therefore, in current work, we have synthesized a hybrid consisting of nanoparticles of HEA and MoS_2. The HEA (Ag-Au-Cu-Pd-Pt) nanoparticles are uniformly decorated on the 2D sheet of MoS_2. The hybrid is further used for gas sensing properties. In order to gain insights into efficient hydrogen sensing, we have performed DFT calculations. It was found that there is a significant structural change at the interface of HEA and MoS_2, due to charge transfer between the two components, which leads to its stability. The hydrogen adsorption was more favourable at HEA sites rather than that at MoS_2, which could explain the enhanced hydrogen gas sensing by HEA- MoS_2 composite.

Experimental

Materials

The Molybdenum disulfide (99%) was obtained from Thermo Fisher Scientific (USA) and used for cryomilling without any processing. Similarly, the metals purchased from Thermo Fisher Scientific (USA), Copper, Silver, Gold, Palladium, and Platinum were used to synthesize HEA NPs using arc melting, followed by the cryomilling process. The DMF(N, N-Dimethylformamide) 99% was also purchased from Thermo Fisher.

Nanoparticles preparation

Equiatomic ($Au_{0.20}Ag_{0.20}Cu_{0.20}Pd_{0.20}Pt_{0.20}$**)** HEA nanoparticles have been prepared using arc melting and casting, followed by the cryomilling method. The all five metals in equal molar ratio have been arc melted and cast as ingot in an inert atmosphere and homogenized at 1000 ^{o}C for 24 h. Subsequently, the cast ingot has been parted into smaller pieces and cryomilled until the formation of finely dispersed nanoparticles, and the detailed process can be found elsewhere[17].

Exfoliation of MoS_2

The MoS_2 powder has also been cryomilled for 7 hours, and the sample has been collected in 2, 4, and 7 hours for characterization. After 7 hours of cryomilling, the MoS_2 powder has been dispersed in 50:50 ratio water/DMF (Dimethylformamide) using ultrasonication. In addition, 1 wt% AgAuCuPdPt HEA nanoparticles also added and sonicated for 30 hours using ultrasonicator operated at 40 Hz, 150 watt for exfoliation of multilayers MoS_2.

Characterizations

The MoS_2 powders have been collected after 2, 4, and 7 hours of cryomillingand characterized using X-ray diffraction (Panalytical, Cu target, λ = 0.154026 nm). The exfoliated MoS_2 in 50:50% DMF/water has been washed with methanol using ultracentrifugation and dispersed in methanol. The one drop of washed and dispersed MoS_2-NPs was placed over a carbon-supported TEM grid (600 mesh Cu) and dried overnight before Transmission Electron

Microscopic (TEM) analysis (FEI, Titan G^2 30-600, operated at 300 kV). Similarly, one drop placed over the glass slide and dried overnight for Raman Spectroscopy analysis using 532 nm laser. The samples were drop casted on to gold-coated glass slides for X-ray Photoelectron spectroscopy (XPS) and Ultraviolet photoelectron spectroscopy (UPS) measurements (Omicron ESCA 2SR XPS system equipped with Mg K_α 1253.6 eV and He I 21.2 eV)

The gas sensing studies have been done in an in house-built sensor characterization system. The details of the system can be found elsewhere[18]. For measuring the sensor properties, the samples suspended in ethanol are drop-casted on the Si substrate, having thermally grown oxide layer and Au interdigitated electrodes deposited by DC sputtering. The sensor current/ resistance is monitored at different temperatures in the presence of various gas concentrations. The sensor response is calculated, as shown in Eq. (1)

$$Sensorresponse\% = \frac{\Delta R}{R} \times 100 \quad \ldots(1)$$

The response was measured for various gases, including Hydrogen, NO_2, NH_3, and volatile Organic Compounds (VOCs). Further, the effect of relative humidity on the response of the sensor was studied by passing the dry air (carrier as well as diluting gas) into bubblers of water maintained in a constant temperature bath.

Computational Methodology

Density functional theory (DFT) was utilized for all theoretical calculations, as implemented in the Vienna ab initio simulation (VASP) software (5.4.1 version)[19]. Electron-ion interactions were described using ultrasoft pseudopotentials[20]. The Perdew-Burke-Ernzerhof (PBE) method of generalized gradient approximation (GGA)[21] was used to approximate the electronic exchange and correlations. A vacuum of 15 Å was kept in the z-direction to avoid spurious interactions between the periodic images.

Results and Discussion

Figure 1(a) shows the schematics of measurement of current/resistance on the exposure of H_2 gas over the surface of MoS_2 nanosheets. The MoS_2 nano-flakes were prepared using inhouse designed low temperature (<123 K) grinding. The layered MoS_2 structure was massively been fractured/exfoliated at extremely low temperature and forms 2D- MoS_2. Subsequently, the nanosheet of MoS_2 decorated using HEA (Ag-Au-Cu-Pd-Pt) NPs allow on its surface. It is confirmed using Raman spectra of MoS_2 nanosheet with and without NPs, as shown in Figure 1b. In the case of HEA NPs decoration, Raman band red shifted by ~2.5 cm^{-1}, which could be due to the functionalization of Ag-Au-Cu-Pd-Pt NPs over MoS_2. The intensity E_{2g} (381 cm^{-1}; in-plane vibration) and A_{1g} (406.7 cm^{-1}; out of plane vibration) of the bulk MoS_2 with MoS_2 nanoflakes after 30 hours sonication shows quite higher intensity. The process of cryomilling in successive hours (2, 4, 7 hours) has progressively led to reduction of the MoS_2 Raman intensity, as shown in Figure S1(a), [Supplementary information] which is considered the evidence of nanostructure formation by cryomilling. In addition, the process of the 7 hours cryomilled followed by 30 hours sonication has led to a drastic decrease of the intensity of E_{2g} and A_{1g} band, as shown in Figure S1(a), which reveals the nanostructured formation with few layers of MoS_2. However, the addition of high entropy alloy nanoparticles (Ag-Au-Cu-Pd-Pt) in 7 hours cryomilled MoS_2 cause of enhancement of the intensity, indicating that the HEA alloy NPs impart surface enhance Raman scattering effects possibly due to electromagnetic field redistribution[22].

The X-ray diffraction (XRD) pattern of MoS_2 nanoflakes with NPs reveals the presence of constituent phases, as shown in Figure 1c. Successive hour of milling as shown in Figure S1(c) [Supplementary information] reveals that the intensity peaks in the XRD pattern continuously decreasing, as the time for cryomilling increases due to massive fracture multilayer MoS_2, which could result in reduced intensity in diffraction pattern as shown in inset of Figure S1(c)

(002) peak. Besides, it was observed that the FWHM of the (002) increases with increasing cryomilling time in Figure S1(c). The photo-absorption (UV-visible) of nanostructured MoS_2 is shown in Figure 1d, and it is found to be weak as compared to that of bulk counterparts[23]. It is further weakening in intensity as milling time increases, as shown in Figure S1(b). The bulk MoS_2 after 30 hours ultrasonication reveals the highest absorbing band at 395, 450, 612 and 674 nm, which can be attributed to near band edge absorption of direct bandgap (rising edge at 700 nm), the four excitonic absorptions (612 (A) and 674 nm (B) near top of valance band and 460 (C) and 395 (D) from deep valance band respectively)[4]. However, the HEA NPs in the methanol show surfaces plasmon resonance band at nearly λ_{max} = 284 nm. Consequently, the combination of MoS_2 decorated with NPs reveals the combined absorption pattern, as shown in Figure1d. The cryomilled MoS_2 with the addition of 30 hours ultrasonication was found continuously decreasing the intensity and increasing the full width at half maxima for 2, 4, and 7 hours of milling, signifying that cryomilling leads to nanostructured MoS_2 with exfoliated in a shorter time of ultrasonication in the solution.

The size and crystallinity of MoS_2 flakes functionalized or decorated with HEA nanoparticles have been estimated using Transmission electron microscopy. Figure 2(a) shows the bright-field TEM image of a few-layer MoS_2 sheets, and Figure 2(b) is selected area electron diffraction pattern of monolayer or few layers MoS_2. The NPs were decorated with MoS_2 as sheen in Figure 2(c) and confirmed by electron ring diffraction pattern shown in Figure 2(d). The high-resolution TEM image of single NPs is shown in Figure 2(e) and Fast Fourier fileted image of HRTEM single nanoparticles shown Figure 2(f), where the plane (111) has been marked and coloured atoms position have been marked for the simple representation of NPs surface (atoms position was not experimentally determined). In addition, chemical homogeneity and composition of nanoparticles have been confirmed with TEM-EDAX

mapping, and energy spectra are shown in Figure 2(g-h), and the inset shows the HAADF image of a nanoparticle.

In order to study the effect of addition of HEA NPs on chemical stoichiometry and electronic structure, the X-ray and UV photoelectron spectroscopy of both the samples were conducted, and the results obtained are analyzed and presented in Figure 3. It is seen from Figure 3(a) that the Mo *3d* core level XPS spectra is quite complex unlike CVD grown single MoS_2 sheets. Several peaks were observed in this region, which have been attributed to core levels of S *2s* and Mo *2p* for Mo^{4+} and Mo^{6+} oxidation states. The peaks are resolved considering the spin orbit coupling for the total angular momentum of Mo 2p 3/2 and 1/2 for each oxidation state. Ideally, for clean, stoichiometric MoS_2, only Mo^{4+} state is expected. However, it is observed that a significantly large Mo^{6+} contribution, which could be resolved clearly in either case i.e. at 229 and 232 eV for 3/2 of Mo^{+4} and Mo^{+6} respectively. The detailed quantification of XPS data is summarized in Table S1 in supporting Information. Moreover, the relative contribution of Mo^{6+} was found to be higher for HEA decorated MoS_2 sample. This implies that there exists a surface or edge oxidation layer on the MoS_2 flakes, which results in the formation of "MoO_3 like" character as found in literature[24, 25]. Similarly, S *2p* core level spectra shown in Figure 3(b) reveals more than one oxidation states for S (S^{2-}, S_2^{2-}) as well. Along with this, metal sulfide peaks could also be seen at lower binding energy i.e.,159.80 eV. In addition to anionic sulfur, several peaks have been found on higher binding energy, which reflects a more positively charged nature of sulfur ions and hence have been attributed to oxidized sulfur i.e., SO_x. Hence, this supports the existence of surface oxidation with observed higher Mo^{6+} ratio in the same.

It is known from the literature that when MoS_2 is made by physical methods such as sputtering, laser ablation, etc. and exposed to air; it results in surface oxidation[25] due to poor crystallinity as well as rather large surface area. Thus, it is important to examine the O *1s* core level in these

samples, and it has been shown in Figure 3(c). Normally, the photoemission from 1s core level of oxygen ion, which is directly or covalently bonded to the metal ion, appears at binding energy 529.5 ± 1 eV. In this case, a peak is observed at 529.6 eV, which corresponds to oxide ion. This could be the oxygen bonded at the edges or surface, as mentioned above and in the literature[15]. However, this peak could be deconvoluted into two peaks i.e., having another peak at higher binding energy than that of 529.5 eV, which could arise because of surface defects, chemisorption etc[26]. This presence of oxide ions are known to give rise to p-type conductivity due to electron withdrawing nature of oxygen[25].

The Ultra Violet (UV) photoelectron Spectroscopy (UPS) was performed to examine the changes in the work function of the sample upon decoration with HEA NPs. As seen in Figure 3(d), as a result of HEA decoration on MoS_2 flakes, the secondary electron cut off is shifted towards higher binding energy, which reflects a lower work function of the HEA decorated sample. The work functions calculated have also been verified using Kelvin Probe system (from KP Technology, UK) at room temperatures, and the values measured are about 4.4 eV and 4.0 eV for bare, and HEA decorated MoS_2. These values are in good agreement with those measured using UPS (photon energy – (Secondary electron cut off – Fermi energy). Thus, it is evident that the HEA nanoparticles affect the electronic transport of the material, which may result in forming a schottky barrier.

Figure 4(a) and 4(b) shows the current–voltage characteristics of pristine MoS_2 and HEA: MoS_2 respectively as a function of temperature. As seen from Figure 4(c) the devices made using Au electrodes show a linear I-V characteristic for pristine MoS_2, as expected[27]. On the other hand, the HEA: MoS_2 shows a nonlinear I-V characteristic indicating a non-ohmic, i.e., schottky nature accompanied with lower conductance of the device. This could be due to a change in the chemical potential of MoS_2 upon decoration with HEA NPs. However, both the devices show semiconducting nature, i.e. the instantaneous resistance decreases upon heating.

Thus, in order to extract the barrier height between at the metal-semiconductor junction in either case, the I-V is analysed for thermionic emission mechanism as it is dominant in absence of any gate voltage (two probe device). Here, the thermionic emission current is given by the following Richardson –Dushman equation (2)[28, 29]

$$I = SA^{*}T^{2}e^{-\frac{q\phi}{kT}}[1 - e^{\frac{qV}{kT}}] \quad (2)$$

Where, I is the current obtained at applied bias V, T is absolute temperature, q is the charge of electron, *k* is Boltzmann constant, *A** is Richardson constant and *S* is the area of the device. The same equation (2) may be written in the form of equation (3) as

$$lnln(I/T^{2}) = lnlnC - \frac{q\phi}{kT}, \quad (3)$$

Where, $C = SA^{*}[1 - e^{\frac{qV}{kT}}]$ (4)

Thus, from Eq (3) when $lnln(I/T^{2})$ is plotted as a function of 1/T, the slope gives the value of barrier height $\phi = |\Phi_{metal} - \Phi_{semiconductor}|$. Ideally, the slope value obtained is further plotted against the value of potential applied to get the y-intercept i.e. in the limit of zero bias[29, 30]. However, we have observed that the slope is practically independent of bias (See Figure S2 in supplementary information) i.e. the barrier is sufficiently high and the change in barrier with application of electric field is minimal. This is also evident from the three orders of magnitude lower current in comparison to that of the ohmic contact formed without HEA nanoparticles.

Thus, the barrier height, ϕ value obtained from Figure 4(d) are 0.195 and 0.35 eVs for bare MoS_2 and HEA decorated MoS_2, respectively. Considering the work function of gold, 5.1 eV, the work function values deduced for bare and HEA decorated MoS_2 are 4.9 and 4.75 eV respectively. These values are in good agreement with those obtained using UPS measurements

and KP measurements. This implies that upon decoration with HEA nanoparticles, the work function of MoS_2 has decreased as already seen from Figure 3(d).

The gas sensing response of the devices was studied using two probes on the exposure of various concentrations of hydrogen gas at different temperatures on the surface of MoS_2+HEA as shown in Figure 1(a). As can be seen from Figure 5(a), the bare MoS_2 without HEA NPs shows fairly low response to 1000 ppm hydrogen gas at room temperature (i.e. 30 ^oC). Nonetheless, the HEA: MoS_2 shows a nearly 10 fold increase in the sensor response when heated to moderate temperatures like 50-80 ^oC. The bare MoS_2 shows consistently low response at all temperatures while, the HEA: MoS_2 sensor response shows a maxima at 80 ^oC and drops when heated beyond. Further, when the response is studied towards various concentrations of hydrogen at various temperatures, it is found to obey power law of semiconductor gas sensors (equation 5)[31], as shown in Figure 5(b).

$$S = AC^{\beta} \tag{5}$$

Here, this equation can be deduced from Fruedlich adsorption isotherm wherein A is a prefactor governing the adsorption kinetics and n is the exponent which depends on surface coverage[32]. Moreover, the HEA NPs when decorated over MoS_2 not only enhance response but also showed improved response time and recovery times. For instance, the comparison of the response and recovery time for pristine MoS_2 and HEA:MoS_2 is shown in Figure 5(c). Here, the response and recovery times are calculated as time required to reach the 90% of the saturation value and 90% under the saturation value respectively. It may be observed from Figure 4(c) that the sensors of pristine MoS_2 and HEA:MoS_2 take 10 min and 15 min as response time while 7 min and 16 min as recovery times respectively.

The Faster response may be due to catalytic activity of the HEA NPs which helps in improving the number as well as rate of the surface adsorption of the target gas molecules. For practical

applications it is ideal that the sensor responds and recovers faster as shown in Figure 5(d) for various concentrations of hydrogen. These obtained time constants with high response are much smaller than those reported to date to the best of our knowledge[10, 29].

Table 1 shows the comparison of the response of MoS_2-HEA device to that of other MoS_2 and noble metal decorated MoS_2 devices reported in the literature. Although the temperature of operation of the MoS_2-HEA device is little higher than room temperature, it shows a vast range of concentration detection limit, i.e., from few ppm to 0.5% H_2 in the air with respectable sensitivity down to ppm level as seen from Figure 5. This could be of practical relevance to leak detection and monitoring ambient levels for safety etc.

Table 1. The comparison of the response of MoS_2-HEA device to that of other MoS_2 and noble metal decorated MoS_2 devices reported in the literature.

Sample composition	**Operating Temperature**	**Gas**	**Selectivity**	**Range**	**Response**	**Response Time (sec)**	**Recovery Time (sec)**	**Reference**
MoS_2 + High entropy Alloys	80	H_2	Yes	20-5000	ΔR/Ra*100= 32% @1000ppm	600 s	420 s	This work
Graphene/ MoS_2 Heterostructure	150	NH_2	NO	10-1000	5% @ 100 ppm	5	40	[29]
		NO_2	NO	0-100	7% @ 5 ppm	5	40	[29]
MoS_2 Nnaowire network	60	NO_2	YES	1-5	ΔR/Ra*100= 18% @5ppm	16	172	[30]
MoS_2/ SnO_2	RT	NO_2	YES	0.5 -10	ΔR/Ra*100= 28% @10ppm	600	100	[31]
MoS_2 with Pt nanoparticles	RT	NH_3	No	1-70	38% @ 70 ppm NH3 &	No saturation in 600 sec	No recovery in 600 s	[32]
		H_2S		10-70	11% @ 70 ppm H2S			
MoS_2 with Pd nanoparticles	RT	H_2	No data	50-10000	35% @10000 ppm H2	2000	1500	[33]
MoS_2 Nanosheets	RT	H_2	No data	10-500	36.5% at 100 ppm	10	6	[34]
Pd-SnO_2-MoS_2	RT	H_2	Moderate	30-5000	15% at 5000 ppm	10	20	[35]

Hydrogen is a reducing gas, i.e., it donates an electron when it surface adsorbs. This electron, when received in an n-type semiconductor, leads to an increase in its carrier concentration and hence resistance drops. While in p-type semiconductors, it recombines with some of the holes and thus decreases the carrier concentration, and hence resistance increases. The rise in resistance observed in this study denotes that the observed behaviour is that of the p-type semiconductor, and this p-type behaviour was attributed to the surface oxygen adsorption on MoS_2 flakes. Further, the type of carriers is also confirmed by hall measurements. The lower work function implies that the fermi level (zero binding energy line) moving closer to the conduction band (away from valance band), which will make the barrier height more for n-type material. On the other hand, the fermi level moving closer to the valance band will make the barrier height higher for p-type semiconductors.

High entropy alloys are solid solutions of five metal atoms, which are otherwise highly catalytically active materials. Whenever such catalytically active metal atoms are attached to semiconductor gas sensor material, it is known to enhance the sensor response by two mechanisms, i.e., controlling the fermi level and spill over mechanism. The Fermi level control results due to changes in electronic transport as a result of the formation of a depletion region, while the spill over refers to the catalytic effect of these particles[36]. The spill over model is described as enhanced adsorption of gaseous species on metals and self-transportation of these species on to the supporting sensor material[37]. Here, the support material does benefit from additional gas species adsorption, which it does not achieve otherwise. The noble metal elements, particularly Pd[38] and alloys of noble metals, enhance the surface adsorption for hydrogen due to such dissociative adsorption of hydrogen atoms[39-41] followed by transfer of adsorbed gas molecules/ atoms to the support materials, i.e. MoS_2 in this case. This transfer

further results in improved charge transfer and hence better catalysis or sensor response. On the other hand, as seen from Figure 4, the electronic levels of the semiconductor are affected upon decoration with metal nanoparticles. At the junction of metal and semiconductor, there exists a barrier due to charge transfer. Metals being strong donors of electrons, these are pumped into the semiconductor. Particularly in case of p-type semiconductors, these electrons recombine with some of the holes, which are majority charge carriers and hence result in restoration of Fermi level towards the intrinsic limit. This increases the resistance of semiconductors, as seen in Figure 4. Further, the formation of nanoscale barriers at the HEA alloy and MoS_2 junctions is beneficial for the sensing as it produces a large change in resistance when there is a small change in carrier concentration of MoS_2 due to hydrogen chemisorption.

Thus, the synergistic effect of all five metal species leads to a giant ten-fold increase in sensor response. Further, the kinetics of surface adsorption decides the sensor response time taken for saturation and recovery. Here, the strong affinity of HEA NPs towards hydrogen results into the faster response as well as recovery of the sensor signal at much lower temperatures than those reported in the literature so far[38]. Moreover, the surface of MoS_2, which is rich in oxygen species after decorating with HEA, further enhances the abundance of active sites for surface adsorption and making it more sensitive.

The response of MoS_2+HEA was studied for various gases like H_2, NO_2, NH_3, and VOC's such as acetone and ethanol for 5000 ppm at 80 ^oC. The response of the material was found to be less than 5% for gases other than H_2 and nearly 40% for H_2 within 10% error bar, as shown in Figure 6(a). This demonstrates the selectivity of the sensor to H_2 at 80 ^oC. Further, the stability of response was studied by measuring the response for the same concentration of gas (5000 ppm) at the same temperature over a period of time. As seen in Figure 6(b), the response is fairly stable over a period of a week, at least. The same response was observed with 10% variance for different samples prepared and measured even after about 4 months.

The response of the material was also studied by varying the Relative Humidity (RH) from 0-80% at 80 °C for 5000 ppm of H_2. The response was almost unaffected over a large range of 0-60% RH, as shown in Figure S3 in supporting information. Subsequently, the response was found to decrease with further increase in the humidity. Moreover, the response at high RH levels is fairly slower compared to that of dry air (0% RH) levels. This could be due to surface passivation, i.e., accumulation of water vapours on the surface of the sensor. This can be overcome by increasing the operating temperature to more than 80 °C preventing from condensation of water vapours as well as its surface adsorption.

To gain atomistic insights into the enhanced gas sensing at the MoS_2-HEA system, density functional theory (DFT) calculations were performed. The optimized lattice parameters of 2D MoS_2 and pristine Pt were found to be: a = b = 3.19 Å, and a = b = c = 3.96 Å, in excellent agreement with previous reports[42]. The AgAuCuPdPt alloy (HEA) special quasirandom structure (SQS) was generated from 5x2x1 supercell of Pt (111) surface using the "mcqs" code employed in Alloy Theoretic Automated Toolkit (ATAT)[43]. The ATAT code employs a Monte Carlo simulated annealing method using an objective function that perfectly matches the maximum number of correlation functions[43]. The SQS generated in such a way mimics the thermodynamic and electronic properties of true structures to a reasonable extent, as has been shown in the earlier reports[44,45]. The unit cell of the SQS (HEA) contained 80 atoms, with the Pt, Pd, Ag, Au, and Cu atoms comprising 20% each of the total composition. The 9x4x1 supercell of MoS_2 was matched with this unit cell of HEA, resulting in a lattice mismatch of 2.4%.

To check the thermodynamic stability of the MoS_2-HEA composite system, interface binding energy was calculated according to the expression[46]:

$$E_b = (E_{MoS_2+HEA} - E_{MoS_2} - E_{HEA})/A \quad \text{(1)}$$

Where E_{MoS_2+HEA}, E_{MoS_2}, and E_{HEA} are the total energies of MoS_2-HEA composite, MoS_2, and HEA, and A is the area of the unit cell (Table S2). The value for E_b was found to be -74.02 meV/Å^2, indicating its high stability, in agreement with the experiments. This is further corroborated by the charge density difference (ρ_{diff}) plot shown in Figure 7(a), which was calculated using:

$$\rho_{diff} = \rho_{MoS_2+HEA} - \rho_{MoS_2} - \rho_{HEA} \quad \text{(2)}$$

Where ρ_{MoS_2+HEA}, ρ_{MoS_2}, and ρ_{HEA} are charge densities of the MoS_2-HEA composite, MoS_2, and HEA, respectively. A significant charge transfer is observed at the interface of MoS_2 and HEA, which indicates large interaction between the two layers and hence the high stability of the composite. To analyze the behaviour of bonding in the composite, electron localization function (ELF) was calculated [47]. The covalent (ELF > 0.5) and metallic bonding (ELF < 0.5) nature of MoS_2 and HEA layers, respectively, are retained after formation of the composite (Figure 7(b), and Figure S5). However, the red regions localized at S atoms (corresponding to their lone pairs) at the interface of MoS_2 and HEA are non-uniform, i.e., its intensity is low where atoms of HEA are closer to MoS_2. It again signifies an appreciable interaction strength between the two layers.

Next, in order to explain the experimental trends observed for response time, H adsorption energy calculations were performed according to the expression given below:

$$E_{H^*} = (E_{tot} - E_{pristine} - \frac{1}{2}E_{H_2})/A \quad \text{(3)}$$

where E_{tot}, $E_{pristine}$, and E_{H_2} are the total energies of H adsorbed system, pristine (bare) system, and isolated H_2 gas molecule, respectively (Table S2). The values for E_{H^*} corresponding to MoS_2 and MoS_2-HEA composite is shown in Figure 7, where it can be seen that E_{H^*} on MoS_2-HEA composite is exothermic, while that on MoS_2 is endothermic. Therefore, H will tend to adsorb faster on MoS_2-HEA composite compared to that on bare MoS_2, hence the response time will be lower for the MoS_2-HEA composite, as is also observed experimentally.

Conclusion

To summarise, we have proposed a facile method to decorate/functionalized 2-D materials. Further, we have investigated its effect on gas sensing properties by comparing with bare MoS_2 that accounts for unusual p-type conduction. The chemical compositional analysis (XPS) has been carried out to account for the unusual p-type conduction in MoS_2. It is evident that both bare MoS_2 and functionalized MoS_2 can be operated at lower temperatures, unlike MOS gas sensors. The calculated values of E_{H^*} from DFT for MoS_2 and functionalized MoS_2 are in good agreement with the experiment and prove that the HEA-functionalized MoS_2 is effective in achieving higher sensitivity than bare MoS_2 with the comparatively lower response and recovery times. Moreover, the MoS_2 +HEA shows excellent selectivity to hydrogen gas. The non-ohmic nature of contact between gold and HEA decorated MoS_2 reveals the potential for enhancement in MoS_2 gas sensing properties.

Acknowledgment
KU and VK would like to thank the DST for the Inspire faculty award grant and IISER TVM central instrumental facility for the XPS-UPS measurements. R.K and A.K.S acknowledge the computational facilities located at Materials Research Centre (MRC), SERC, and Solid State

Structural and Chemistry Unit (SSCU), at Indian Institute of Science, Bangalore and DST-Korea for funding.

References:

1. E. Yalon, C. J. McClellan, K. K. H. Smithe, M. Muñoz Rojo, R. L. Xu, S. V. Suryavanshi, A. J. Gabourie, C. M. Neumann, F. Xiong, A. B. Farimani and E. Pop, *Nano Letters*, 2017, **17**, 3429-3433.
2. T. Stephenson, Z. Li, B. Olsen and D. Mitlin, *Energy Environ. Sci.*, 2014, **7**, 209-231.
3. Y. Jiao, A. M. Hafez, D. Cao, A. Mukhopadhyay, Y. Ma and H. Zhu, *Small*, 2018, **14**, 1800640.
4. J. Huang, X. Deng, H. Wan, F. Chen, Y. Lin, X. Xu, R. Ma and T. Sasaki, *ACS Sustain. Chem. Eng.*, 2018, **6**, 5227-5237.
5. W. Zhang, P. Zhang, Z. Su and G. Wei, *Nanoscale*, 2015, **7**, 18364-18378.
6. D. Tyagi, H. Wang, W. Huang, L. Hu, Y. Tang, Z. Guo, Z. Ouyang and H. Zhang, *Nanoscale*, 2020, **12**, 3535-3559.
7. F. K. Perkins, A. L. Friedman, E. Cobas, P. M. Campbell, G. G. Jernigan and B. T. Jonker, *Nano Letters*, 2013, **13**, 668-673.
8. T. Hübert, L. Boon-Brett, V. Palmisano and M. A. Bader, *Int. J. Hydrogen Energ.*, 2014, **39**, 20474-20483.
9. Y. Luo, C. Zhang, B. Zheng, X. Geng and M. Debliquy, *Int. J. Hydrogen Energ.*, 2017, **42**, 20386-20397.
10. D. J. Late, Y.-K. Huang, B. Liu, J. Acharya, S. N. Shirodkar, J. Luo, A. Yan, D. Charles, U. V. Waghmare, V. P. Dravid and C. N. R. Rao, *ACS Nano*, 2013, **7**, 4879-4891.
11. Y. Niu, R. Wang, W. Jiao, G. Ding, L. Hao, F. Yang and X. He, *Carbon*, 2015, **95**, 34-41.
12. J.-S. Kim, H.-W. Yoo, H. O. Choi and H.-T. Jung, *Nano Letters*, 2014, **14**, 5941-5947.
13. A. S. Sharma, S. Yadav, K. Biswas and B. Basu, *Mater. Sci. Eng. R Rep*, 2018, **131**, 1-42.
14. E. P. George, D. Raabe and R. O. Ritchie, *Nat. Rev. Mater.*, 2019, **4**, 515-534.
15. N. K. Katiyar, S. Nellaiappan, R. Kumar, K. D. Malviya, K. G. Pradeep, A. K. Singh, S. Sharma, C. S. Tiwary and K. Biswas, *Mater. Today Energy*, 2020, **16**, 100393.
16. S. Nellaiappan, N. K. Katiyar, R. Kumar, A. Parui, K. D. Malviya, K. G. Pradeep, A. K. Singh, S. Sharma, C. S. Tiwary and K. Biswas, *ACS Catalysis*, 2020, **10**, 3658-3663.
17. N. Kumar, C. S. Tiwary and K. Biswas, *J. mater. Sci.*, 2018, **53**, 13411-13423.
18. S. Suresh, K. M. B. Urs, A. T. Vasudevan, S. Sriram and V. B. Kamble, *physica status solidi (RRL) – Rapid Research Letters*, 2019, **13**, 1800683.
19. G. Kresse and J. Hafner, *Phys. Rev. B*, 1993, **47**, 558-561.
20. D. Vanderbilt, *Phys. Rev. B*, 1990, **41**, 7892-7895.
21. J. P. Perdew, K. Burke and M. Ernzerhof, *Physical Review Letters*, 1996, **77**, 3865-3868.
22. W. Li, P. H. C. Camargo, X. Lu and Y. Xia, *Nano Letters*, 2009, **9**, 485-490.
23. M.-L. Tsai, S.-H. Su, J.-K. Chang, D.-S. Tsai, C.-H. Chen, C.-I. Wu, L.-J. Li, L.-J. Chen and J.-H. He, *ACS Nano*, 2014, **8**, 8317-8322.
24. Z. Yin, X. Zhang, Y. Cai, J. Chen, J. I. Wong, Y.-Y. Tay, J. Chai, J. Wu, Z. Zeng, B. Zheng, H. Y. Yang and H. Zhang, *Angew. Chem. Int. Ed.*, 2014, **53**, 12560-12565.
25. A. T. Neal, R. Pachter and S. Mou, *Applied Physics Letters*, 2017, **110**.
26. V. B. Kamble, S. V. Bhat and A. M. Umarji, *J. Appl. Phys.*, 2013, **113**, 244307.

27. S. McDonnell, R. Addou, C. Buie, R. M. Wallace and C. L. Hinkle, *ACS Nano*, 2014, **8**, 2880-2888.
28. M. Grundmann, *The Physics of Semiconductors*, Springer-Verlag Berlin Heidelberg, 2 edn., 2010.
29. B. Liu, L. Chen, G. Liu, A. N. Abbas, M. Fathi and C. Zhou, *ACS Nano*, 2014, **8**, 5304-5314.
30. J.-R. Chen, P. M. Odenthal, A. G. Swartz, G. C. Floyd, H. Wen, K. Y. Luo and R. K. Kawakami, *Nano Letters*, 2013, **13**, 3106-3110.
31. V. B. Kamble and A. M. Umarji, *Sens. Actuators B Chem.*, 2016, **236**, 208-217.
32. P. Atkins and J. d. Paula, *Atkins' Physical Chemistry*, OUP Oxford, 2010.
33. B. Cho, J. Yoon, S. K. Lim, A. R. Kim, D.-H. Kim, S.-G. Park, J.-D. Kwon, Y.-J. Lee, K.-H. Lee, B. H. Lee, H. C. Ko and M. G. Hahm, *ACS Appl. Mater. Interfaces*, 2015, **7**, 16775-16780.
34. R. Kumar, N. Goel and M. Kumar, *Appl. Phys. Lett.*, 2018, **112**, 053502.
35. S. Cui, Z. Wen, X. Huang, J. Chang and J. Chen, *Small*, 2015, **11**, 2305-2313.
36. V. B. Kamble and A. M. Umarji, *RSC Advances*, 2015, **5**, 27509-27516.
37. R. Prins, *Chemical Reviews*, 2012, **112**, 2714-2738.
38. K. Zhang, T. H. Lee, J. H. Cha, H. W. Jang, M. Shokouhimehr and J.-W. Choi, *Electron. Mater. Lett.*, 2019, **15**, 727-732.
39. V. B. Parambhath, R. Nagar, K. Sethupathi and S. Ramaprabhu, *The Journal of Physical Chemistry C*, 2011, **115**, 15679-15685.
40. P. Badenes, L. Daza, I. Rodriguez-Ramos and A. Guerrero-Ruiz, *Stud. Surf. Sci. Catal.*, 1997, **112**, 241-250.
41. C. Liu, Q. Kuang, Z. Xie and L. Zheng, *CrystEngComm*, 2015, **17**, 6308-6313.
42. A. Singh and A. K. Singh, *Phys. Rev. B*, 2019, **99**, 121201.
43. A. van de Walle, P. Tiwary, M. de Jong, D. L. Olmsted, M. Asta, A. Dick, D. Shin, Y. Wang, L. Q. Chen and Z. K. Liu, *Calphad*, 2013, **42**, 13-18.
44. C. Jiang, C. R. Stanek, K. E. Sickafus and B. P. Uberuaga, *Phys. Rev. B*, 2009, **79**, 104203.
45. K. C. Hass, L. C. Davis and A. Zunger, *Phys. Rev. B*, 1990, **42**, 3757-3760.
46. R. Kumar, D. Das and A. K. Singh, *J. Catal.*, 2018, **359**, 143-150.
47. A. Savin, O. Jepsen, J. Flad, O. K. Andersen, H. Preuss and H. G. von Schnering, *Angew. Chem. Int. Ed.*, 1992, **31**, 187-188.

Figures

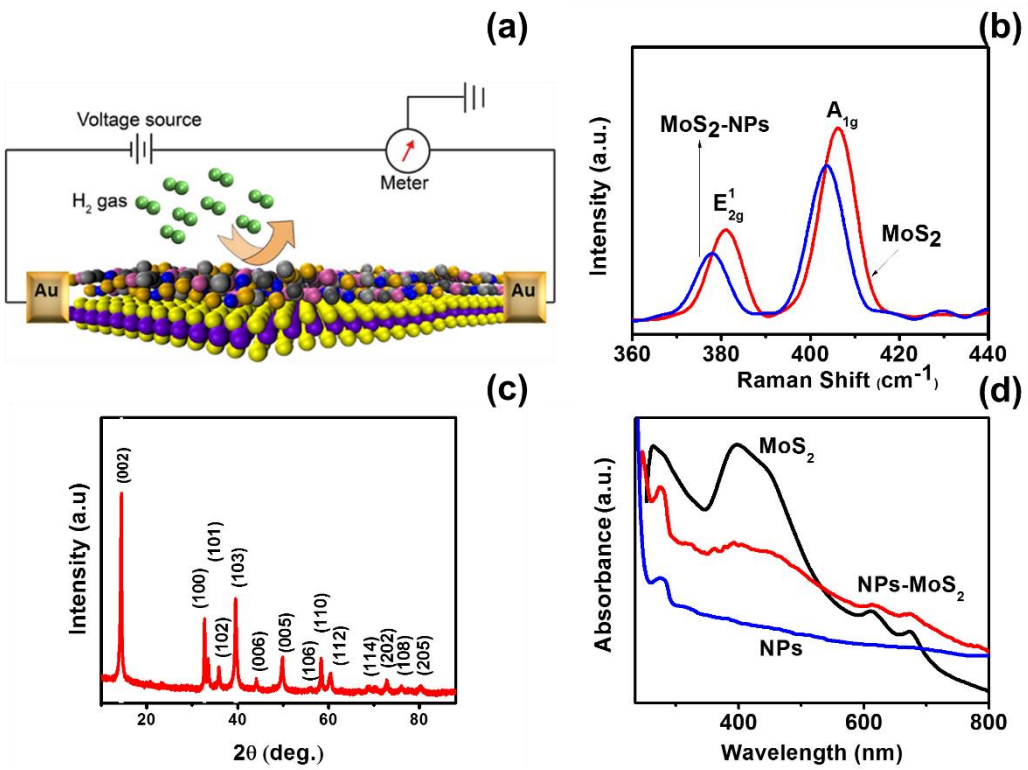
(a)
Voltage source
Meter
H_2 gas
Au
Au
(b)
MoS_2-NPs
A_{1g}
E^1_{2g}
MoS_2
Intensity (a.u.)
360
380
400
420
440
Raman Shift (cm^{-1})
(c)
Intensity (a.u)
(002)
(100)
(101)
(102)
(103)
(006)
(005)
(106)
(110)
(112)
(114)
(202)
(108)
(205)
20
40
60
80
2θ (deg.)
(d)
MoS_2
NPs-MoS_2
NPs
Absorbance (a.u.)
400
600
800
Wavelength (nm)

Figure 1 (a) Schematics of device used for sensing consisting the materials architecture (MoS_2-decorated with HEA (Ag-Au-Cu-Pd-Pt) alloy nanoparticles **(b)** Raman spectrum of MoS_2 with and without HEA (Ag-Au-Cu-Pd-Pt) **(c)** X-ray diffraction pattern of the HEA decorated MoS2 **(d)** absorbance spectra of MoS_2 , HEA NPs and HEA-NPs decorated MoS_2.

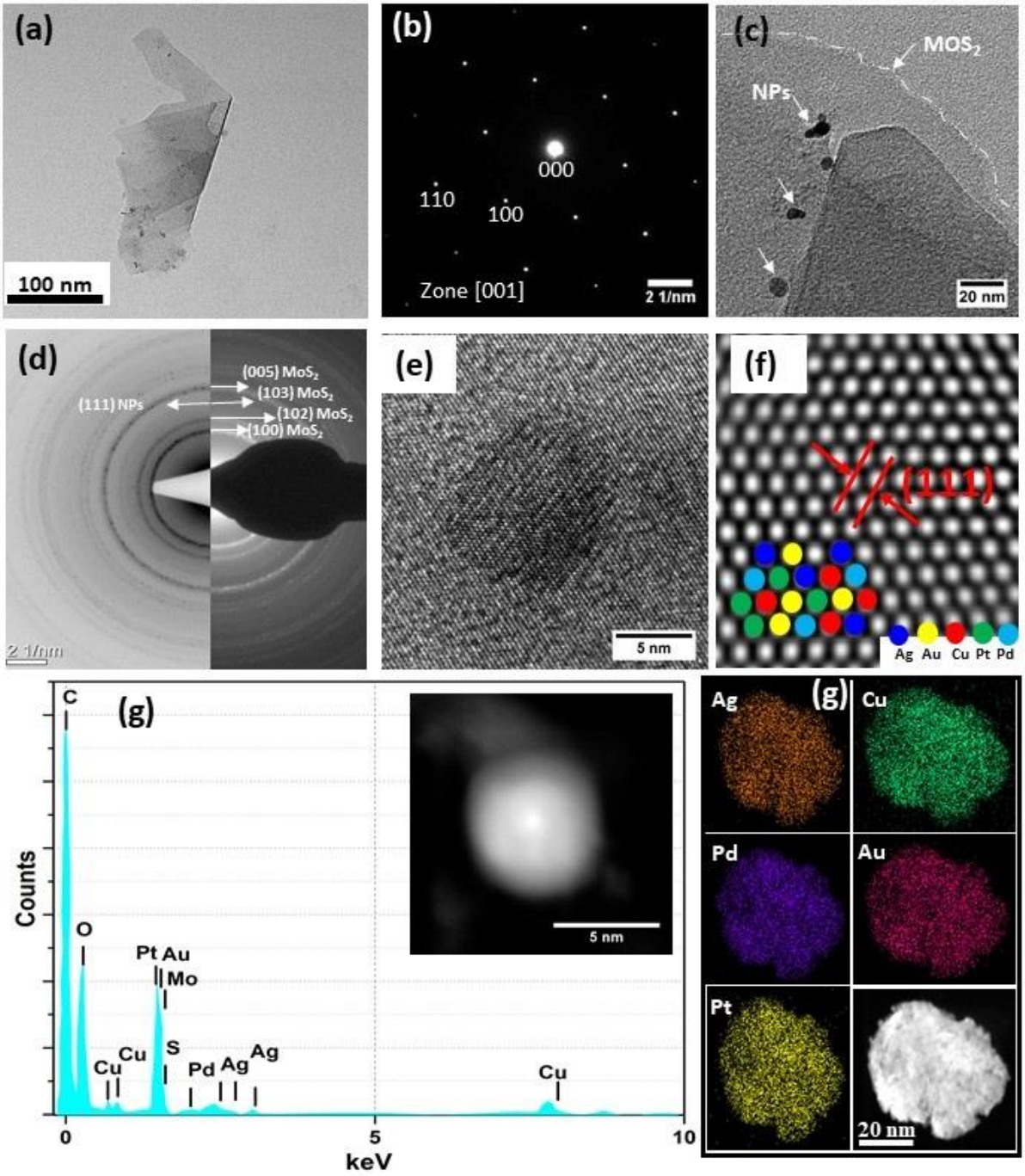

Figure 2: (a) TEM Bright field image of MoS_2 **s**heet **(b)** SAED pattern of MoS_2 sheet **(c)** TEM Bright field image of MoS_2 sheet decorated with HEA NPs **(d)** corresponding electron ring diffraction pattern **(e)** HRTEM image of HEA (Ag-Au-Cu-Pd-Pt) on MoS_2 sheet **(f)** FFT filtered HRTEM image of HEA NPs **(g)** EDAX pattern inset shows single nanoparticles HAADF image **(h)** elemental mapping of HEA NPs.

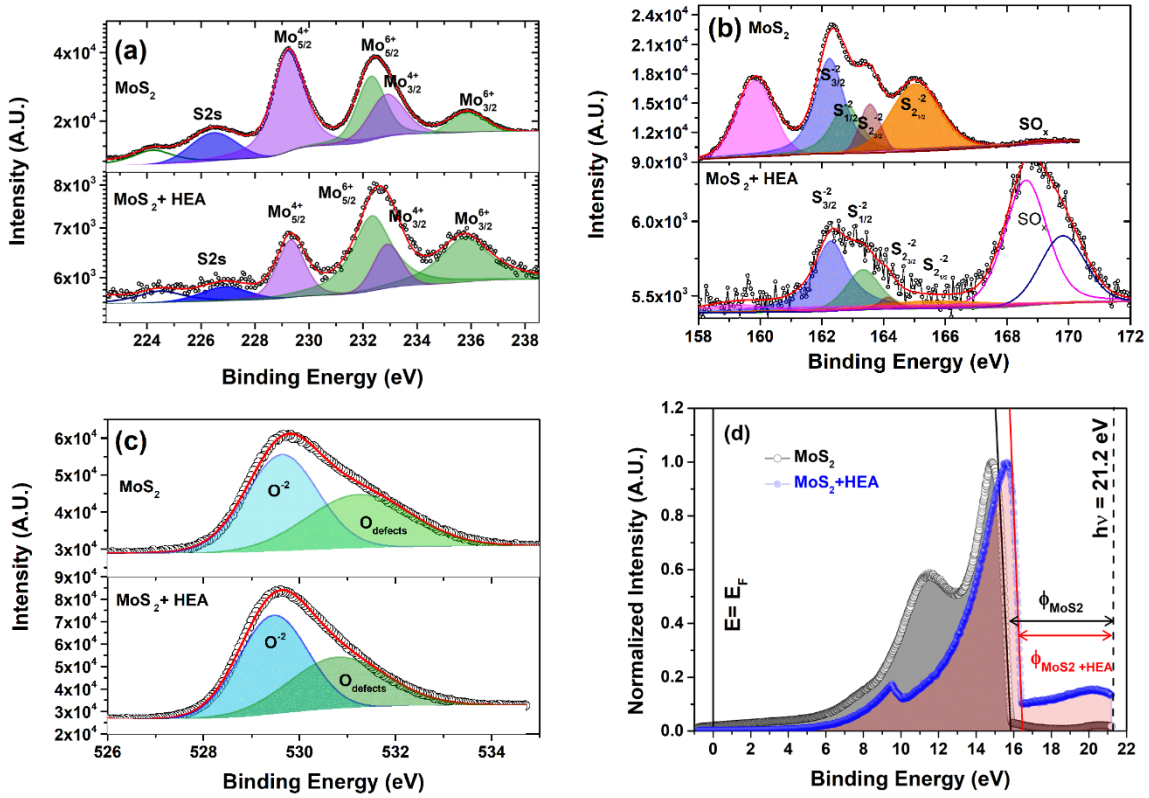

Figure 3: The X-ray photoelectron spectra of **(a)** Mo 3d- S 2s, **(b)** S 2p, **(c)** O 1s core levels and **(d)** UV photoelectron spectra of MoS_2 and MoS_2-HEA.

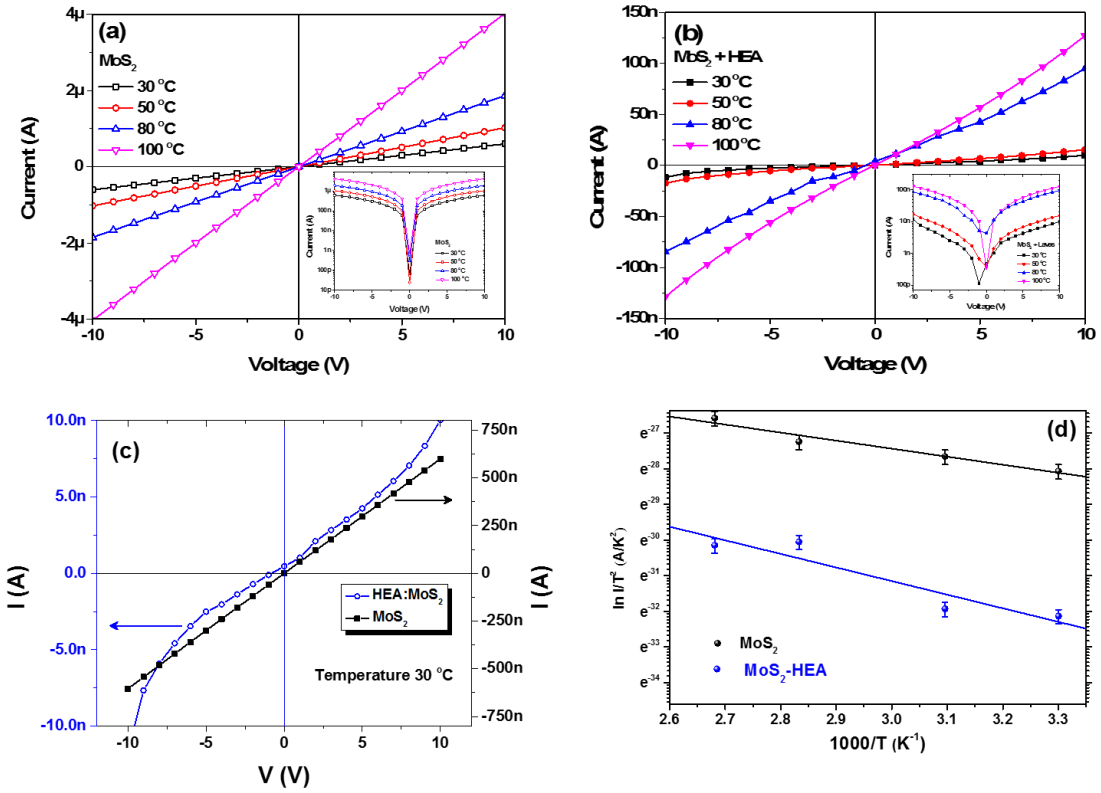

Figure 4: The current-voltage (I-V) characteristics of devices fabricated using **(a)** only MoS_2 and **(b)** HEA NPs decorated MoS_2 as a function of temperature. **(c)** the comparison of linearity and current of both devices at 30 OC. **(d)** the Arrhenius plot of ln (I/T^2) vs 1000/T for both the samples.

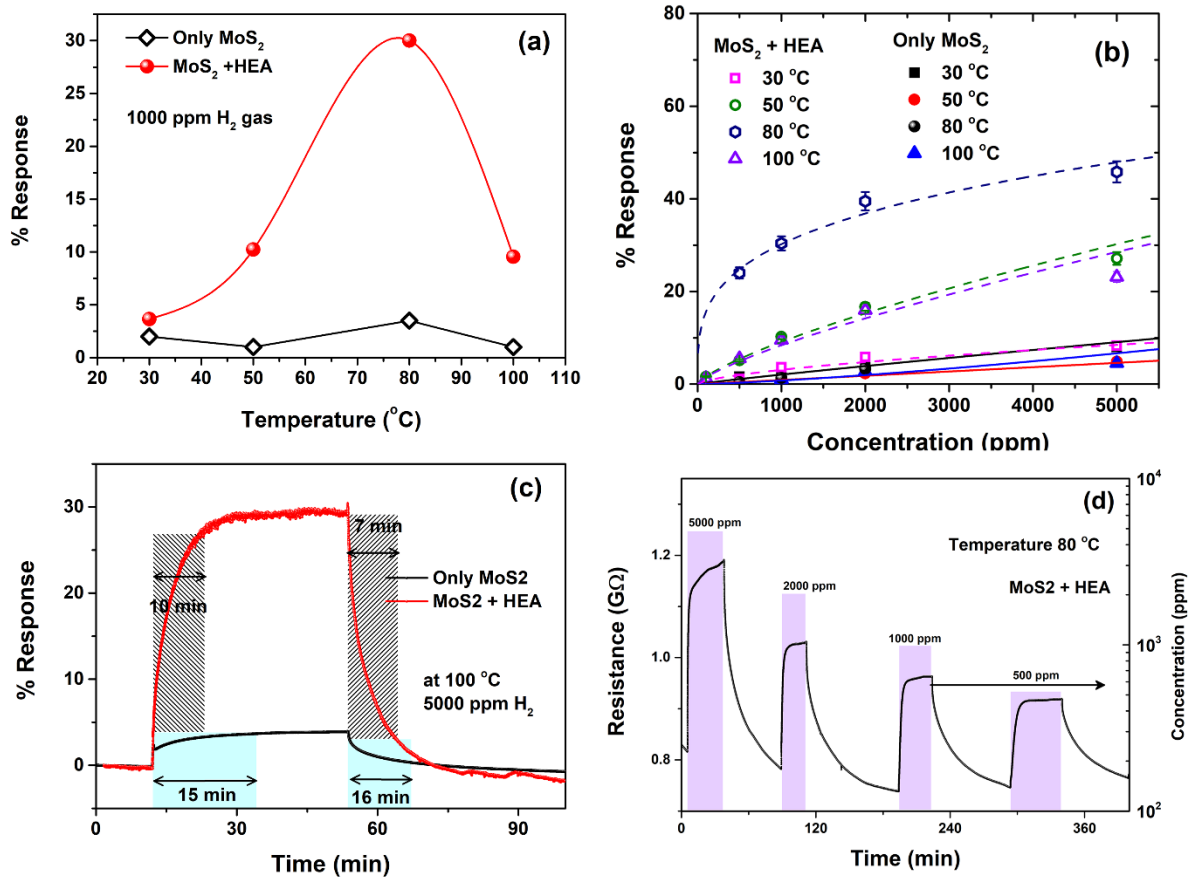

Figure 5: The comparison of sensor response only MoS_2 and HEA NPs decorated MoS_2 with **(a)** temperature and **(b)** hydrogen gas concentration. The lines show power law fit. **(c)** The comparison of response time and recovery times for 5000 ppm H_2 gas at 100°C. **(d)** The typical response of HEA NPs decorated MoS_2 at 80°C for various concentrations.

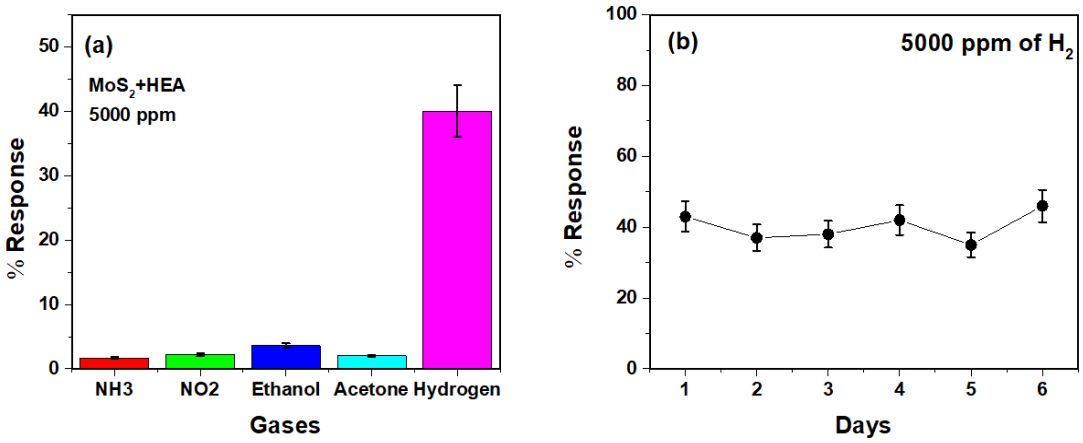

Figure 6. (a) The response of the MoS_2+HEA sample to various gases showing selectivity to H_2 at 80 °C for 5000 ppm. **(b)** The stability of the response to H_2 at 80 °C for 5000 ppm.

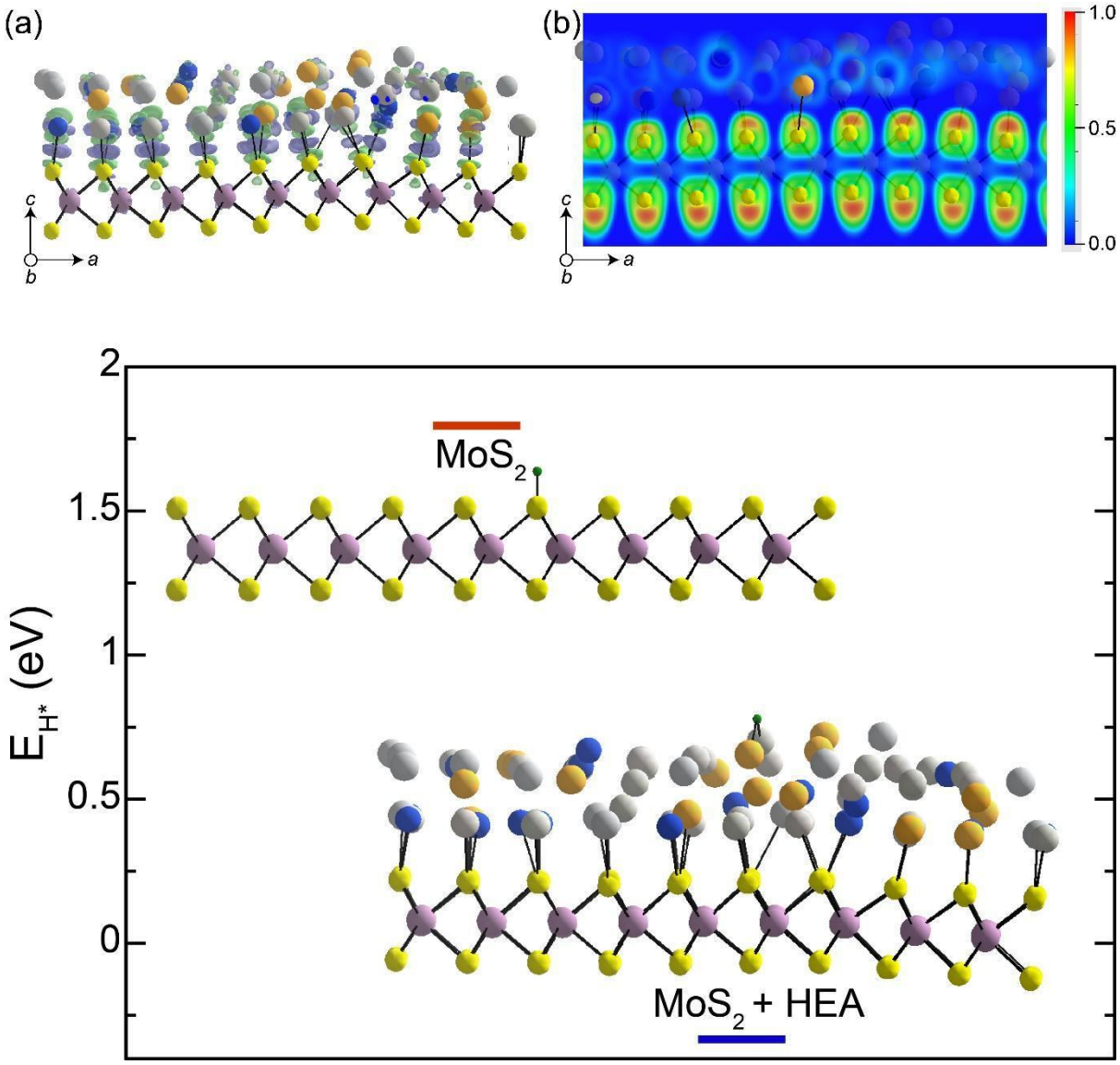

Figure 7. (a) Charge density difference plotted for MoS_2-HEA system. The charge accumulation and depletion regions are indicated by lime green and dark violet isosurfaces, respectively. The isosurface value has been set to $4x10^{-3}$ eÅ^{-3}. ***(b)*** ELF plot for MoS_2-HEA system along (010) plane. The color bar for ELF values are also shown alongside. The light violet, yellow, light grey, dark grey, gold, silver, blue, and green spheres represent Mo, S, Pt, Pd, Au, Ag, Cu, and H atoms, respectively. ***(c)*** E_{H^*} of MoS_2 (red solid line) and MoS_2-HEA (blue solid line) systems. The completely optimized H-adsorbed structures are also shown where light violet, yellow, light grey, dark grey, gold, silver, blue, and green spheres represent Mo, S, Pt, Pd, Au, Ag, Cu, and H atoms, respectively.